Conference paper

Vit Prokop*, Lukas Strizik*, Jiri Oswald, Milan Vlcek, Ludvik Benes, Spyros N. Yannopoulos, Bozena Frumarova and Tomas Wagner

1.5 μm photoluminescence and upconversion photoluminescence in GeGaAsS:Er chalcogenide glass

https://doi.org/10.1515/pac-2018-1231

Abstract: The paper reports on ≈1.5 μm Stokes photoluminescence (PL) emission and upconversion photoluminescence (UCPL) emission in the visible and near-infrared spectral region in Er^{3+}-doped $Ge_{25}Ga_8As_2S_{65}$ chalcogenide glasses at pumping wavelengths of 980 and 1550 nm. The ≈1.5 μm PL emission spectra are broadened with increasing concentration of Er ions which is discussed in terms of radiation trapping and UCPL dynamics affecting the Er^{3+}: $^4I_{13/2}$ level lifetime. The UCPL emission was observed at ≈530, ≈550, ≈660, ≈810 and ≈990 nm and its overall intensity as well as red-to-green UCPL emission intensity ratio increases with increasing Er concentration. To explore the UCPL dynamics we measured double logarithmic dependency of green (≈550 nm) and red (≈660 nm) UCPL emission versus pump power at pumping wavelength of 975 nm. Moreover, we measured quadrature frequency resolved spectroscopy (QFRS) on green UCPL emission (≈550 nm) using 975 nm pumping wavelength and various excitation powers. The QFRS spectra on green UCPL were analyzed in term of QFRS transfer function for three-level model from which we deduced energy transfer upconversion rate w_{11} (s^{-1}) originating from Er^{3+}: $^4I_{11/2}$, $^4I_{11/2} \rightarrow {}^4F_{7/2}$, $^4I_{15/2}$ transitions.

Keywords: chalcogenide glasses; energy transfer upconversion; Er-doped glasses; excited state absorption; photoluminescence; quadrature frequency resolved spectroscopy; SSC-2018; upconversion dynamics; upconversion photoluminescence.

Article note: A collection of invited papers based on presentations at the 13th International Conference on Solid State Chemistry (SSC-2018), Pardubice, Czech Republic, September 16–21, 2018.

***Corresponding authors: Vit Prokop and Lukas Strizik,** Department of General and Inorganic Chemistry, Faculty of Chemical Technology, University of Pardubice, Studentska 573, Pardubice 532 10, Czech Republic, Tel.: +420 466 037 000, E-mail: vit.prokop@student.upce.cz (V. Prokop); lukas.strizik@upce.cz (L. Strizik)
Jiri Oswald: Institute of Physics of the Czech Academy of Sciences v.v.i., Cukrovarnicka 10, 162 00, Prague 6, Czech Republic
Milan Vlcek: Institute of Macromolecular Chemistry of the AS CR, v.v.i., Heyrovskeho nam. 2, 162 00, Prague 6, Czech Republic
Ludvik Benes: Joint Laboratory of Solid State Chemistry, Faculty of Chemical Technology, University of Pardubice, Pardubice 532 10, Czech Republic
Spyros N. Yannopoulos: Foundation for Research and Technology-Hellas, Institute of Chemical Engineering Sciences (FORTH/ICE-HT), P.O. Box 1414, GR-26504 Patras, Greece
Bozena Frumarova: Center of Materials and Nanotechnology, Faculty of Chemical Technology, University of Pardubice, nam. Cs. legii 565, Pardubice 530 02, Czech Republic
Tomas Wagner: Department of General and Inorganic Chemistry, Faculty of Chemical Technology, University of Pardubice, Studentska 573, Pardubice 532 10, Czech Republic; and Center of Materials and Nanotechnology, Faculty of Chemical Technology, University of Pardubice, nam. Cs. legii 565, Pardubice 530 02, Czech Republic

© 2019 IUPAC & De Gruyter. This work is licensed under a Creative Commons Attribution-NonCommercial-NoDerivatives 4.0 International License. For more information, please visit: http://creativecommons.org/licenses/by-nc-nd/4.0/

Introduction

Amorphous chalcogenides doped with rare-earth (RE) ions are promising materials in many applications due to their unique properties [1–3] such as low phonon energy, high refractive index, broad transparency from the visible to the mid-infrared spectral region with relatively good solubility of RE^{3+} ions in chalcogenide glasses (ChG) containing Ga [4], Al [5], In [6]. ChG can be relatively easily prepared as bulks or thin films and in variety of shapes [1].

Among the most studied and promising chalcogenide hosts for RE^{3+} doping to achieve the visible UCPL belong sulfides as Ge-Ga-S [7], Ge-Ga-Sb-S [8], Ge-Ga-As-S [9], and Ga-La-S [10]. Compared to Ge-Ga-S glasses, the glasses of the Ge-Ga-As-S system show improved glass-forming ability [9] and thermal stability [8, 11] with still good solubility of RE^{3+} ions [9]. The Ge-Ga-Sb-S glasses have higher thermal stability compared to Ge-Ga-As-S however, their transparency is markedly reduced in the visible spectral region [8, 12, 13]. Studied materials show potential for optical fibers [14], optical fiber amplifiers [15], non-linear optical waveguides [16], laser devices [17, 18] or chemical sensors and detectors [19, 20].

In this article we present photoluminescent and structural properties of Er^{3+}-doped $Ge_{25}Ga_8As_2S_{65}$ (GGAS) chalcogenide glasses as promising candidates for UCPL from the green visible to the near-infrared spectral region. We measured emission spectra and lifetimes of ≈1.5 μm PL Stokes emission and UCPL emission spectra at pumping wavelengths of 980 and 1550 nm. Moreover, the green UCPL emission (≈550 nm) at 975 nm pumping wavelength and various pump powers was investigated by QFRS to deduce the energy transfer upconversion rate parameter w_{11} for 0.01 and 0.5 % Er-doped GGAS glasses.

Experimental

GGAS: x at% Er^{3+} chalcogenide glasses, where $x = 0.01$–1 at%, were synthesized by the melt-quenching technique from high purity elements of Ge (5N), Ga (5N), As (5N), S (4N) and Er (3N). The synthesis was carried out in the rocking furnace at 1050 °C for 24 h. Melt was quenched into water and ampoule with raw glass was subsequently annealed near the glass transition temperature $(T_g - 20)$ °C for 3 h to relax the mechanical strain. After that, the glass samples were slowly cooled down to room temperature, cut into ≈1 mm thick rectangles and both-side polished into the optical quality.

The amorphous state of Er^{3+}-doped GGAS glasses was studied by X-ray diffraction (XRD) analysis using diffractometer Bruker AXS D8 Advance with Cu $K\alpha$ radiation in the range of 2θ from 10° to 70°. The chemical composition of prepared samples was determined by the energy dispersive X-ray (EDX) microanalyzer IXRF System with a detector GRESHAM Sirius 10 and at accelerating voltage of the primary electron beam ≈20 kV. The room temperature Raman spectra were measured by the Raman FRA-106 Bruker as a part of the FT-IR spectrophotometer IFS 55 using the excitation source of the YAG: Nd^{3+} laser (λ_{exc} ≈1064 nm) in the 50–200 cm^{-1} spectral region. The Raman spectra were reduced by the method of Gammon and Shuker [21] and then decomposed by a sum of eight Gaussians using the Fityk program v. 0.9.8 [22].

The refractive index n_G of the glasses was analyzed by the variable angle spectroscopic ellipsometry VASE®, J.A. Woollam Co., Inc. in the spectral region of 500–2300 nm measured with a step of 20 nm and at angles of light incidence 65°, 70° and 75°. Ellipsometric data were fitted to the Sellmeier model, $n_G^2 = A + B\lambda^2/(\lambda^2 - C)$ [23]. The concentration of Er^{3+} ions ρ (cm^{-3}) in glassy samples was calculated from density measurements and chemical composition. Transmittance T was measured by double-beam UV-Vis-NIR spectrophotometer JASCO V-570 in the spectral region of 400–1800 nm with step of 1 nm. The absorption cross-section σ_a spectrum was calculated by the equation $\sigma_a = \ln 10\,[-\log T + \log(1 - R)]/\rho d$, where R is reflectance determined from refractive index as $R = [(n_G + 1)/(n_G - 1)]^2$ and d is sample thickness in cm units. The absorption cross-section spectrum of 0.5 % Er-doped GGAS glass was used for application of Judd–Ofelt (JO) theory to calculate the intensities of Er^{3+} intra-4f electronic transitions. Er^{3+} ≈1.5 μm PL emission spectra were acquired at pumping wavelength of 980 nm, the UCPL emission spectra in the spectral region of 400–1050 nm were acquired at 980 nm (~9 W cm^{-2}) and 1550 nm (~13 W cm^{-2}) excitation wavelengths using the diode lasers.

The Er^{3+}: ${}^4I_{13/2}$ level lifetimes (at $\lambda \approx 1535$ nm) for Er-doped GGAS glasses excited by 980 nm were analyzed by time-resolved spectroscopy from $1/e$ value or by using the Eq. 1:

$$N_1 = N_1(0)e^{-k_1 t} + N_2(0)\frac{\beta k_2}{k_1 - k_2}(e^{-k_2 t} - e^{-k_1 t}), \quad (1)$$

where $N_i(0)$ is the initial population density, k_i is relaxation rate at level ${}^4I_{13/2}$ ($i=1$) and ${}^4I_{11/2}$ ($i=2$), β is branching ratio of the ${}^4I_{11/2} \rightarrow {}^4I_{13/2}$ transitions and t is time. Equation 1 takes into account the delayed population of the ${}^4I_{13/2}$ energy level from the pumped ${}^4I_{11/2}$ level.

The QFRS spectra on green UCPL emission ($\lambda \approx 550$ nm) were measured at pumping wavelength of 975 nm and at various pump powers using the QFRS system specified in the previous articles [7, 24, 25], except that we replaced the focusing lens to focal length of ≈25 mm and we used photomultiplier (PMT) tube Hamamatsu H10723-20 as a detector preset to 0.7 V. The QFRS spectra were acquired at various pump powers ranging from 0.79 to 42.5 mW. Pump power $P \approx 1$ mW corresponds to photon-flux density $\Phi \sim 2.9 \times 10^{21}$ cm^{-2} s^{-1}. The excitation power dependence of green (≈ 550 nm) and red (≈ 660 nm) UCPL emission was measured by the same instrument using the lock-in detection at chopping frequency of 30 Hz.

Results and discussion

Figure 1a presents the XRD diffractograms of 0.5 and 1.0 % Er-doped GGAS samples. The samples doped with 0.5 and less at% of Er^{3+} ions are amorphous however, the 1 at% Er-doped sample is partially crystalline as indicate the sharp diffraction lines in Fig. 1a. This is also suggested by SEM images of GGAS samples doped with 0.5 or 1 at% of Er ions (Fig. 1c and d) where the presence of at least two phases in heavily Er-doped sample is observed. The presence of crystallites in 1 at% Er-doped GGAS sample is also featured by sharp-shaped Er^{3+}: ${}^4I_{13/2} \rightarrow {}^4I_{15/2}$ (≈ 1.5 μm) emission spectrum presented in Fig. 1b due to appearance of Stark levels thus indicating that the crystalline phase occurs in close proximity to the Er^{3+} ions [26, 27].

The experimentally determined chemical composition of all Er-doped GGAS samples shown in Table 1 agrees well with theoretical composition. However, as presented by SEM image of Fig. 1d, the heavily

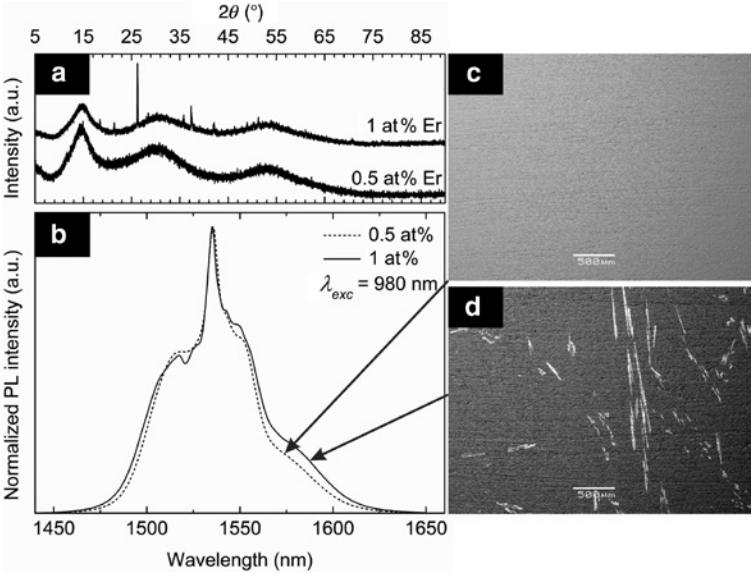

Fig. 1: Effect of Er content on glass-forming ability.
(a) XRD diffractograms, (b) Er^{3+}: ${}^4I_{13/2} \rightarrow {}^4I_{15/2}$ (~1.5 μm) PL emission spectra under 980 nm excitation and (c, d) SEM images for the respective 0.5 at% and 1 at% Er-doped GGAS samples.

Table 1: The chemical composition of the synthesized GGAS:Er samples determined by the EDX spectroscopy.

Er in $Ge_{25}Ga_8As_2S_{65}$	Chemical composition				
	Ga (at%)	Ge (at%)	As (at%)	S (at%)	Er (at%)
0.01 at%	7	26	2	65	–
0.1 at%	7	26	2	65	–
0.5 at%	7	26	2	65	–
1 at% (light phase)	4	12	1	64	19
1 at% (dark phase)	7	26	2	65	–

The experimental error is ±1 at%.

Er-doped sample contains two phases: dark phase and light phase. The chemical composition of dark phase corresponds to theoretical chemical composition of prepared glasses however, the light phase is Er-enriched phase (see Table 1). Thus, the Er solubility limit in $Ge_{25}Ga_8As_2S_{65}$ glasses lies between 0.5 and 1 at% of Er ions which agrees well with the previously published work [27], where for the homogenous distribution of RE ions in chalcogenide glasses the Ga/RE atomic ratio is proposed to be ≥10.

The structure of the GGAS glass was investigated by the Raman scattering. A representative reduced Raman spectrum shown in the Fig. 2 was decomposed to 8 Gaussian-type lines centered approximately at 159, 281, 331, 345, 375, 412, 439 and 485 cm^{-1}. An attempt to interpret the origin of these lines to specific vibrational modes is based on previous works [28–33]. The bands at 159, 345 and 412 cm^{-1} can be assigned to corner-sharing ν_4, ν_1 and ν_3 vibrations of the [GeS_4] tetrahedra, while contributions forming the corresponding modes of the [GaS_4] tetrahedra cannot be excluded. The band at 375 cm^{-1} is assigned to ν_1-[GeS_4] and [GaS_4] vibrations of edge-shared tetrahedral units. This line is practically the companion ν_1^c vibration mode related to edge-shared tetrahedral of [GeS_4] at 370 cm^{-1}. The band at 281 cm^{-1} can be assigned to the vibrational mode of the $S_3Ge(Ga)$-$Ge(Ga)S_3$ structural units containing homonuclear (semi)metal–(semi)metal bonds. The band centered at 331 cm^{-1} could be possibly assigned to ν_1-[GaS_4] vibrations of tetrahedral units. The band at 439 cm^{-1} is still an unsolved issue, but could be probably assigned to companion ν_3^c vibration modes related to edge-shared tetrahedral units [GeS_4] and [GaS_4]. The band around 485 cm^{-1} has been assigned to the existence of disulfide bonds (or two-membered S chains) in form of S_2As-S-S-As_2S and $S_3Ge(Ga)$-S-S-$Ge(Ga)S_3$.

Figure 3 presents absorption-cross section spectrum of Er^{3+} in GGAS glass composed of seven Er^{3+} absorption bands. These bands are attributed to ground state absorption (GSA) transitions from Er^{3+}: $^4I_{15/2}$ to Er^{3+}: $^4I_{13/2}$ (≈1552 nm), $^4I_{11/2}$ (≈991 nm), $^4I_{9/2}$ (≈817 nm), $^4F_{9/2}$ (≈666 nm), $^4S_{3/2}$ (≈552 nm), $^2H_{11/2}$ (≈530 nm) and $^4F_{7/2}$ (≈491 nm) levels. The inset of the Fig. 3 shows the dispersion of refractive index of GGAS:Er^{3+} measured by spectroscopic ellipsometry in transparent spectral region. The refractive index is practically identical for all studied samples ($n_G \approx 2.10$ at $\lambda = 1550$ nm), except that of 1 at% Er-doped sample which was partially crystalline and therefore was not analyzed.

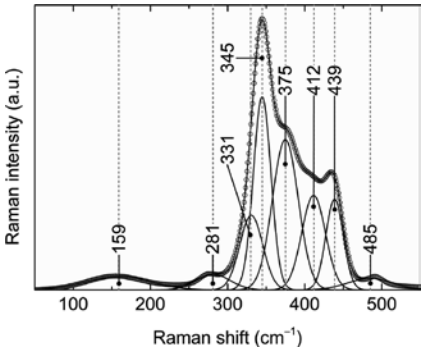

Fig. 2: Reduced Raman spectrum of the GGAS glass. Open circles are experimental data, bold black line is sum of Gaussians used for spectrum decomposition.

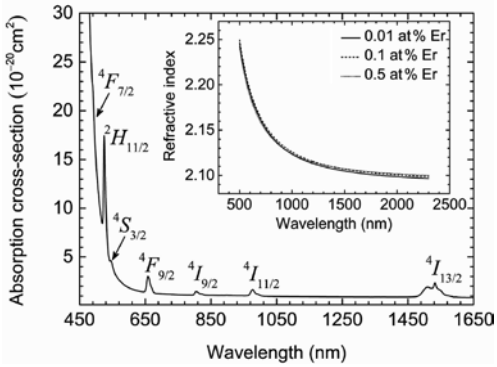

Fig. 3: GSA cross-section spectrum of the 0.5 at% Er-doped GGAS glass. Inset: Dispersion of refractive index for GGAS glasses doped with 0.01, 0.1 and 0.5 at% of Er.

Figure 4a and b show normalized absorption and emission spectra of the Er^{3+}: $^4I_{13/2} \leftrightarrow {}^4I_{15/2}$ ($\lambda \approx 1.5$ µm) transitions in GGAS glasses at pumping wavelength of 980 nm. The ≈1.5 µm emission band is broadened with increasing concentration of Er ions, while the absorption band of all studied glasses samples exhibits no significant changes in shape. For better understanding of this behavior, lifetimes of Er^{3+}: $^4I_{13/2}$ energy level as a function of Er concentration in GGAS glasses were analyzed. The decay curves of the $^4I_{13/2} \rightarrow {}^4I_{15/2}$ transitions under 980 nm pumping wavelength are presented in Fig. 4c. The Er^{3+}: $^4I_{13/2}$ level lifetime $\tau = 1/k_1$ was analyzed by fitting of decay curves in Fig. 4c using the Eq. 1 with fixed parameters of $k_2 = 696$ s^{-1} and $\beta = 0.136$ which were obtained by Judd–Ofelt theory with inclusion of multiphonon relaxation rate [24]. Lifetime values determined by using Eq. 1 or from $1/e$ values are presented in the inset of Fig. 4c. It can be seen that lifetimes determined from $1/e$ values are notably higher than those obtained by using the Eq. 1 nevertheless, they holds same trends. The Er^{3+}: $^4I_{13/2}$ lifetime value $\tau \approx 2.76$ ms determined by Eq. 1 for 0.01% Er-doped GGAS sample matches better the lifetime $\tau^{JO} \approx 2.16$ ms calculated by Judd–Ofelt theory than that $\tau \approx 3.35$ ms determined from $1/e$ value. The $^4I_{13/2}$ lifetime is firstly prolonged with increasing Er concentration from 0.01 to 0.1 at% and subsequently decreases with further increase of Er content. However, the mechanism behind this is still unclear. The lifetime may be prolonged e.g. due to radiation trapping processes [34–36] or by cross-relaxation CR2 processes Er^{3+}: $^2H_{11/2}$, $^4I_{15/2} \rightarrow {}^4F_{9/2}$, $^4I_{13/2}$ [37, 38]. Contrary to that, the lifetime shortening may be explained by the concentration quenching [39] or by the Er^{3+}: $^4I_{11/2}$, $^4I_{13/2} \rightarrow {}^4F_{9/2}$, $^4I_{15/2}$ energy transfer upconversion ETU2 processes [40–43]. The considerable presence of cross-relaxation and energy transfer upconversion processes is discussed later in the manuscript.

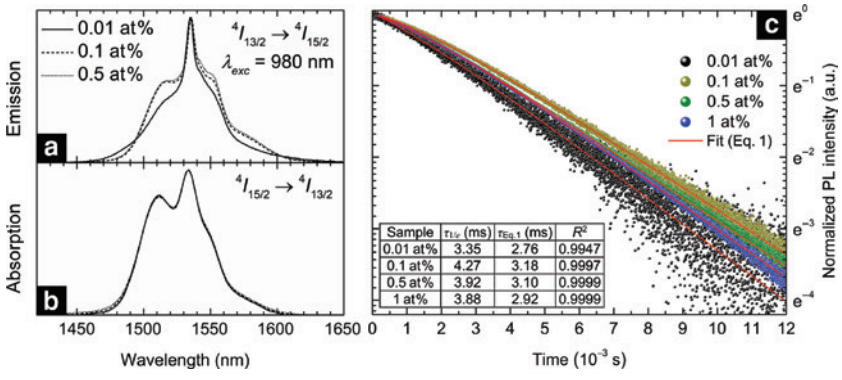

Fig. 4: Er concentration dependence on the $^4I_{15/2} \leftrightarrow {}^4I_{13/2}$ transitions.
(a, b) Are respective normalized emission and absorption spectra of the Er^{3+}: $^4I_{13/2} \leftrightarrow {}^4I_{15/2}$ transitions in GGAS:Er glass under 980 nm pumping wavelength. (c) The decay curves of Er^{3+}: $^4I_{13/2} \rightarrow {}^4I_{15/2}$ transitions in GGAS glass under 980 nm excitation; inset: $^4I_{13/2}$ lifetimes determined from $1/e$ values $\tau_{1/e}$ or by using the Eq. 1 $\tau_{Eq.1}$ with maximal error of ±0.05 ms. (Color online).

Upconversion photoluminescence (UCPL) emission spectra at pumping wavelengths of 980 or 1550 nm are presented in Fig. 5. There are observed five emission bands originating from electronic transitions from Er^{3+} upper levels of $^2H_{11/2}$ (≈530 nm), $^4S_{3/2}$ (≈550 nm), $^4F_{9/2}$ (≈660 nm), $^4I_{9/2}$ (≈810 nm) and $^4I_{11/2}$ (≈990 nm) to Er^{3+}: $^4I_{15/2}$ ground level. The overall UCPL emission intensity as well as red-to-green UCPL emission intensity ratio, i.e. ratio of the red UCPL emission intensity of the Er^{3+}: $^4F_{9/2} \rightarrow {}^4I_{15/2}$ (≈660 nm) transitions to that of the green UCPL emission intensity of the Er^{3+}: $^2H_{11/2}/^4S_{3/2} \rightarrow {}^4I_{15/2}$ (≈530 + 550 nm) transitions, increases with increasing Er^{3+} concentration. Such behavior may be explained by the exploration of the UCPL dynamics.

There are three basic UCPL mechanisms adopted in literature [44]: (I) ground state absorption (GSA) followed by excited state absorption (ESA), i.e. GSA/ESA; (II) ground state absorption (GSA) followed by energy transfer upconversion (ETU), i.e. GSA/ETU; and (III) ground state absorption (GSA) followed by cross-relaxation (CR) processes, i.e. photon avalanche (PA) upconversion. The GSA/ESA mechanism may originate within single Er^{3+} ion thus, it is independent on the Er–Er interionic distance [44]. In contrast, the GSA/ETU or PA UCPL requires energy transfer between two neighboring Er^{3+} ions therefore they are dependent on the interionic distance which is usually adjusted by concentration of Er^{3+} ions inside of a host matrix [44]. Since the green UCPL emission intensity increases rapidly and nonlinearly with increasing concentration of Er^{3+} ions, the additional GSA/ETU mechanism to GSA/ESA may stay behind the UCPL dynamics in highly Er-doped GGAS glasses, i.e. mixed GSA/ESA + ETU [44, 45]. Thus, we investigated the green UCPL dynamics (λ≈550 nm) using the QFRS for three-level model approximation (see Fig. 7) at pump wavelength of 975 nm and various pump powers P (mW) or photon-flux densities Φ ($cm^{-2}\,s^{-1}$). Further details can be found in the recently published paper [24].

The double logarithmic dependency of UCPL emission intensity versus pump power is presented for green and red UCPL emission in Fig. 6 and comprises of two linear segments, where the slope of each segment provides the number of photons involved in the UCPL process [44]. Theoretically, the slope n of low-power linear segment is $n = 2$ for both GSA/ESA and GSA/ETU UCPL mechanisms, and it scales as $n = 1 - 2$ for GSA/ESA or $n = 1$ for GSA/ETU processes at high-power region [44]. The low-power and high-power linear segments are divided by a kink point P_k (or Φ_k) which was found to be ~3 mW for green UCPL and ~2.8 mW for red UCPL. The experimentally determined slope values $n \approx 2$ at $P < P_k$ indicate a presence of two-photon UCPL processes.

The energy transfer rate parameter w_{11} (s^{-1}) of the Er^{3+}: $^4I_{11/2}$, $^4I_{11/2} \rightarrow {}^4F_{7/2}$, $^4I_{15/2}$ transition for green UCPL may be analyzed by QFRS on green UCPL at pump powers below P_k in combination with three-level model [24, 44]. Figure 7 shows the P-evolved QFRS spectra of the green UCPL for the 0.01 (a) and 0.5 % (b) Er-doped GGAS glasses measured from pump powers P ~ 0.79 to 42.5 mW or photon-flux densities from $\Phi \sim 2.3 \times 10^{21}$ to 1.2×10^{23} $cm^{-2}\,s^{-1}$. The QFRS spectra plotted as a function of lifetime τ (s) in logarithmic scale are double-peaked, where long-lifetime component τ_1 corresponds to Φ-evolved relaxation rate $R_1(\Phi) = 1/\tau_1(\Phi)$ at the intermediate level $^4I_{11/2}$ and short-lifetime component τ_2 to Φ-evolved relaxation rate $R_2(\Phi) = 1/\tau_2(\Phi)$ at the upper coupled manifolds $^4F_{7/2}/^2H_{11/2}/^4S_{3/2}$. The lifetime distributions were obtained by deconvolution of QFRS

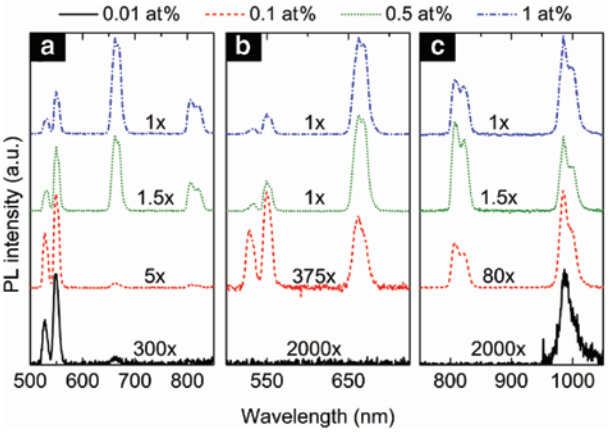

Fig. 5: UCPL emission spectra of the Er^{3+} doped GGAS chalcogenide glasses excited. (a) By the 980 nm or (b and c) 1550 nm laser. (Color online).

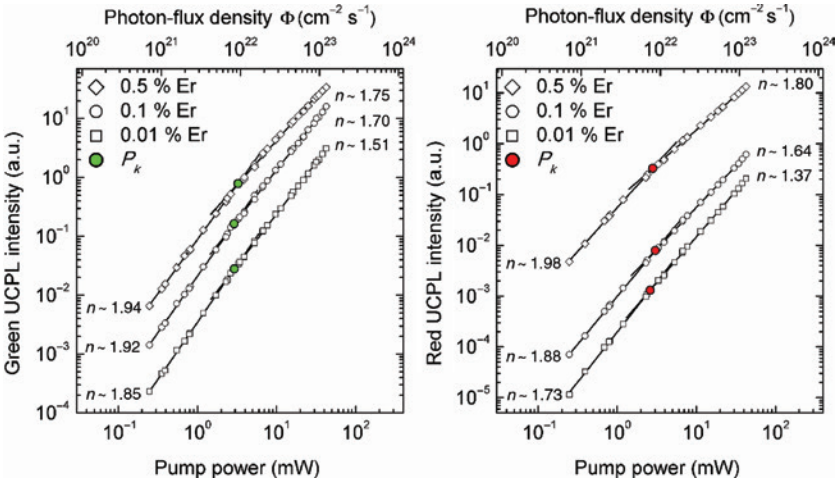

Fig. 6: The double logarithmic plots of green (≈550 nm) and red (≈660 nm) UCPL emission intensity vs. pump power at pumping wavelength of 975 nm.

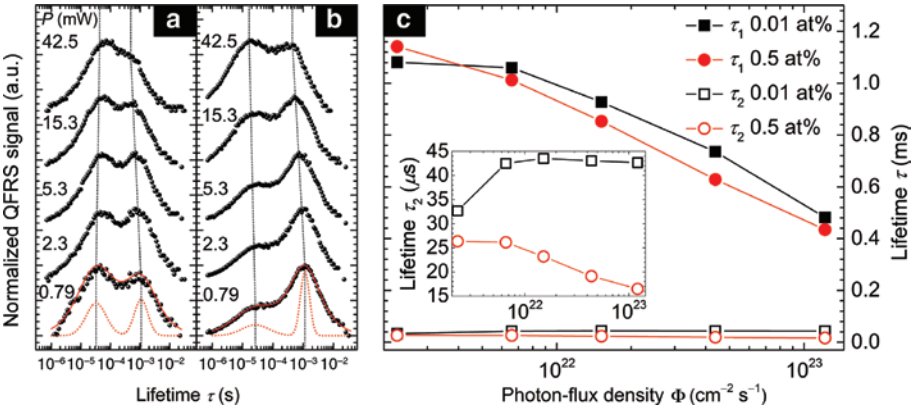

Fig. 7: QFRS spectroscopy.
P-evolved QFRS spectra of the green UCPL for the (a) 0.01 at% and (b) 0.5 at% Er-doped GGAS glasses measured under 975 nm excitation. (c) Φ-evolved lifetimes τ_1 and τ_2 for 0.01 and 0.5 at% Er-doped GGAS glasses under 975 nm pumping wavelength; inset: Detail of Φ-evolved τ_2.

spectra by a linear combination of two Gaussians. The τ_1 component is rapidly shortened with increasing Φ from ≈1.14 to ≈0.43 ms while τ_2 component is less sensitive to change of Φ with lifetime value of ~10 μs (Fig. 7c). Theoretically, the presence of mixed GSA/ESA + ETU process is featured by significant growth of the peak at τ_2 component compared to peak at τ_1 component with increasing Φ [24] which was observed experimentally in heavily 0.5 at% Er-doped GGAS sample (see Fig. 7).

Moreover, from QFRS spectra presented in Fig. 7 may be observed that the short lifetime τ_2 rapidly decreased in heavily Er-doped GGAS sample. This may be explained by the closer proximity of fundamental absorption edge to thermally coupled Er^{3+} energy levels $^4F_{7/2}/^2H_{11/2}/^4S_{3/2}$ (see Fig. 3) allowing the energy transfer processes from Er^{3+} ions to a host matrix [24, 25]. At certain low Φ, the energy transfer parameter w_{11} may be analyzed by the ratio $\gamma\ (\Phi \to 0)$ expressed by Eq. 2, which is ratio between peak a_2 at the short-lifetime component τ_2 and peak a_1 at the long-lifetime component τ_1 [24]:

$$\gamma(0) = \left(1 - \frac{k_1}{k_2}\right)\left(1 + \frac{2w\sigma_0}{k_1\sigma_1}\right)^{-1} - \frac{k_1}{k_2}, \tag{2}$$

where $k_1 = R_1(\Phi \to 0)$ and $k_2 = R_2(\Phi \to 0)$ are relaxation rates at the intermediate and upper coupled energy levels, respectively, σ_0 is GSA cross-section and σ_1 is ESA cross-section. We approximated the $\gamma(0)$ ratio utilizing

the parameters a_1, a_2, k_1, k_2 analyzed from the QFRS spectra at $\Phi < \Phi_k$ ($P \sim 0.79$ mW). To derive the energy transfer rate w_{11} (s^{-1}) from ratio $\gamma(0)$, the knowledge of σ_0 and σ_1 is required as well. These parameters were obtained by using Judd–Ofelt (JO) theory [46–50] with resulting JO intensity parameters $\Omega_2 = (13.02 \pm 0.07) \times 10^{-20}$ cm^2, $\Omega_4 = (3.41 \pm 0.08) \times 10^{-20}$ cm^2 and $\Omega_6 = (1.48 \pm 0.03) \times 10^{-20}$ cm^2 from which were subsequently calculated $\sigma_0 = 6.6 \times 10^{-20}$ cm^2 and $\sigma_1 = 10.9 \times 10^{-20}$ cm^2 values. We found that the parameter $w_{11} = 40$ s^{-1} for the 0.01 % Er-doped GGAS sample and $w_{11} = 2960$ s^{-1} for the 0.5 % Er-doped GGAS glass. These parameters are slightly higher than those obtained for GeGaS:Er glasses [24] which is however attributed to energy transfer processes from Er^{3+}: $^4F_{7/2}/^2H_{11/2}/^4S_{3/2}$ levels to a host matrix due to their merging [24, 25] as is evident in Fig. 3. This is also supported by the extraordinary low values of short-lifetime component [25] $\tau_2 \approx 33$ µs for 0.01 % Er-doped sample and $\tau_2 \approx 26$ µs for 0.5 % Er-doped sample at the lowest Φ in comparison with lifetime value obtained by JO theory of $\tau_2(\mathrm{JO}) \approx 168$ µs.

The increase of red-to-green UCPL emission intensity under 980 nm pumping wavelength with increasing Er concentration Fig. 8a may be explained on the basis of energy level model approximation depicted in Fig. 8b in accordance with Refs. [25, 40–43, 51–55] as following. At low Er concentrations, the ETU or CR processes may be neglected [44]. Thus, the green emitting levels $^4F_{7/2}/^2H_{11/2}/^4S_{3/2}$ are populated mainly via GSA/ESA processes, while the Er^{3+}: $^4F_{9/2}$ energy level may be populated by the radiative and/or nonradiative recombination from excited Er^{3+}: $^4F_{7/2}/^2H_{11/2}/^4S_{3/2}$ levels or by the radiative and/or nonradiative recombination from Er^{3+}: $^4I_{11/2}$ to $^4I_{13/2}$ followed by ESA process Er^{3+}: $^4I_{13/2} \rightarrow {}^4F_{9/2}$ [25]. As a result, the green UCPL emission dominates over red UCPL emission at low concentrations of Er ions, as was observed in Fig. 8a. However, at higher concentrations of Er ions, the ETU and CR processes become pronounced and may significantly modify above mentioned dynamics. In the case of green UCPL emission, there is proposed Er^{3+}: $^4I_{11/2}$, $^4I_{11/2} \rightarrow {}^4F_{7/2}$, $^4I_{15/2}$ energy transfer [24] which was studied by the QFRS mentioned above. This ETU process significantly promotes the green UCPL emission intensity with increasing Er concentration. However, in the case of red UCPL emission, the red-emitting level $^4F_{9/2}$ may be populated by the Er^{3+}: $^4I_{11/2}$, $^4I_{13/2} \rightarrow {}^4F_{9/2}$, $^4I_{15/2}$ energy transfer and Er^{3+}: $^4F_{7/2}$, $^4I_{11/2} \rightarrow {}^4F_{9/2}$, $^4F_{9/2}$ CR1 processes [43, 53–55] or by the Er^{3+}: $^2H_{11/2}/^4S_{3/2}$, $^4I_{15/2} \rightarrow {}^4I_{9/2}$, $^4I_{13/2}$ CR2 followed by ESA2 or ETU2 processes [42, 51, 52]. Since 3–4 photons are required to obtain green (~530 + 550 nm) and red (~660 nm) UCPL emission at pumping wavelength of 1550 nm, the UCPL mechanism is more complex. In low Er^{3+}-doped samples, the green-emitting levels ($^2H_{11/2}$, $^4S_{3/2}$) are populated via the sequential GSA/ESA $^4I_{15/2} \rightarrow {}^4I_{13/2} \rightarrow {}^4I_{9/2} \rightarrow {}^2H_{11/2}/^4S_{3/2}$ transitions and the red-emitting level $^4F_{9/2}$ by the subsequent radiative or nonradiative recombination $^2H_{11/2}/^4S_{3/2} \rightarrow {}^4F_{9/2}$ or by the

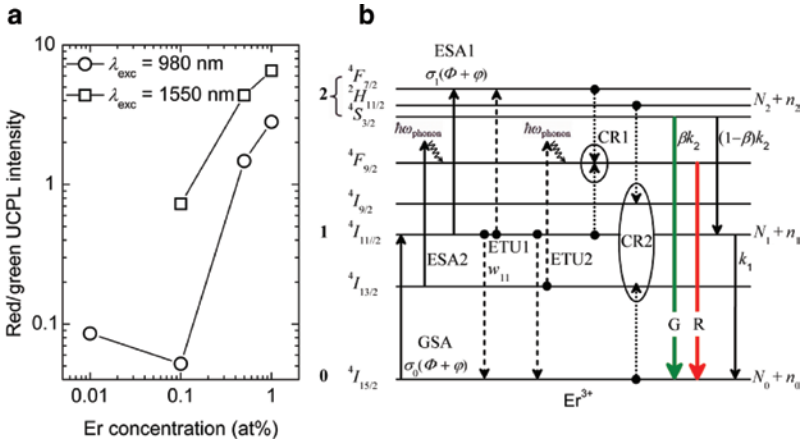

Fig. 8: Green and Red upconversion photoluminescence.
(a) Red-to-Green UCPL emission intensity ratio versus Er^{3+} concentration in GGAS at pumping wavelength of 980 and 1550 nm, (b) Schematic of energy-level diagram for green and red UCPL emission at pumping wavelength of 975 nm; the curved arrows indicate the multiphonon relaxation routes; N_i represent population densities with perturbed population densities n_i at energy level i originating from a sinusoidal modulation φ of continuous-wave photon-flux density Φ; β is branching ratio under three-level model approximation. (Color online).

phonon-assisted $^4I_{15/2} \rightarrow {}^4I_{13/2} \rightarrow {}^4I_{9/2} \rightarrow {}^4I_{11/2}$ + phonon $\rightarrow {}^4F_{9/2}$ GSA/ESA transitions. In contrast to 980 nm excitation wavelength, the red-to-green UCPL emission intensity ratio is higher for samples excited by 1550 nm which suggests the presence of phonon-assisted GSA/ESA processes mentioned above leading to population of red-emitting level Er^{3+}: $^4F_{9/2}$. The presence of the phonon-assisted process "$^4I_{9/2} \rightarrow {}^4I_{11/2}$ + phonon" is also supported by the higher UCPL emission intensity of the Er^{3+}: $^4I_{11/2} \rightarrow {}^4I_{15/2}$ (~990 nm) transitions compared with the Er^{3+}: $^4I_{9/2} \rightarrow {}^4I_{15/2}$ (~810 nm) UCPL (see Fig. 5c). In heavily Er-doped samples the red UCPL emission dominates over the green UCPL emission which may be attributed to the presence of additional energy transfer Er^{3+}: $^4I_{13/2}$, $^4I_{11/2} \rightarrow {}^4I_{15/2}$, $^4F_{9/2}$ populating the red-emitting level $^4F_{9/2}$. Such energy transfer process should depopulate the Er^{3+}: $^4I_{11/2}$ level thus decrease the Er^{3+}: $^4I_{11/2} \rightarrow {}^4I_{15/2}$ (~990 nm) UCPL emission intensity which is really lower in comparison with the Er^{3+}: $^4I_{9/2} \rightarrow {}^4I_{15/2}$ (~810 nm) UCPL intensity in the 0.5 % Er-doped GGAS glass (see Fig. 5c). Moreover, the UCPL emission spectrum for 1 % Er-doped sample in Fig. 5c shows higher UCPL emission intensity at ~990 nm compared with those at ~810 nm which suggests the possible presence of additional cross-relaxation processes Er^{3+}: $^4I_{13/2}$, $^4S_{3/2} \rightarrow {}^4I_{11/2}$, $^4F_{9/2}$ and Er^{3+}: $^4I_{9/2}$, $^4S_{3/2} \rightarrow {}^4F_{9/2}$, $^4F_{9/2}$ all populating the red-emitting level $^4F_{9/2}$ [56–59]. So mostly, the red-emitting level is populated at the expense of population of green emitting level under the both 980 and 1550 nm excitation wavelengths [60]. Therefore, red-to-green UCPL emission intensity ratio increases with increasing Er concentration.

Conclusions

We studied structural properties, ≈1.5 μm Stokes and upconversion photoluminescence in Er-doped $Ge_{25}Ga_8As_2S_{65}$ glasses at pumping wavelengths of 980 and 1550 nm. Since the 1 at% Er-doped GGAS sample was partially crystalline with Er-enriched phase and those doped 0.5 at% remained amorphous, it may be deduced that the Er solubility limit in studied glasses lies between 0.5 and 1 at%. The broadening of the Er^{3+}: $^4I_{13/2} \rightarrow {}^4I_{15/2}$ ($\lambda \approx 1.5$ μm) emission spectrum under 980 nm excitation and change of $^4I_{13/2}$ lifetime with increasing concentration of Er ions was discussed in terms of radiation trapping and upconversion processes. Upconversion photoluminescence was observed from visible green to near-infrared spectral region at pumping wavelength of 980 and 1550 nm. The overall UCPL emission intensity as well as red-to-green UCPL emission intensity ratio increases with increasing Er concentration which was discussed by changes of the UCPL dynamics including the energy transfer and the cross-relaxation processes at higher content of Er ions. The green UCPL emission ($\lambda \approx 550$ nm) was studied by the QFRS spectroscopy under 975 nm excitation and at various pump powers in term of QFRS transfer function for three-level model from which the energy transfer upconversion parameter w_{11} was deduced. The double-peaked QFRS spectra are composed of two lifetime components where the long-lifetime component $\tau_1 \approx 1.14–0.43$ ms reflects the relaxation at the intermediate level Er^{3+}: $^4I_{11/2}$ while the short lifetime component τ_2 of several tens of μs reflects the relaxation rate at coupled energy levels $^4F_{7/2}/^2H_{11/2}/^4S_{3/2}$. The green UCPL dynamics in 0.01 at% Er-doped GGAS glass is mainly driven via the GSA/ESA processes while that in 0.5 at% Er-doped sample contains mixed GSA/ESA + ETU processes which is manifested by the greater energy transfer upconversion rate parameter $w_{11} = 2960$ s^{-1} for 0.5 % Er-doped samples compared to negligible ETU rate $w_{11} = 40$ s^{-1} for 0.01 % Er-doped sample. Such ETU rate parameters are slightly higher than those reported for GeGaS:Er glasses which is explained by the additional energy transfer processes from Er^{3+} ions to a host matrix due to merging of Er^{3+}: $^4F_{7/2}/^2H_{11/2}/^4S_{3/2}$ green emitting levels with fundamental absorption of a host matrix. Nevertheless, the GeGaAsS:Er glasses are promising candidates for UCPL applications as they have improved glass-forming ability and thermal properties compared to GeGaS:Er glasses and higher visible transparency than GeGaSbS:Er glasses.

Acknowledgements: This work was supported by the project CZ.1.05/4.1.00/11.0251 and by grant LM2015082 Center of Materials and Nanotechnologies from the Czech Ministry of Education, Youth and Sports of the Czech Republic and European Regional Development Fund-Project High sensitive sensors and low density materials based on polymeric nanocomposites – NANOMAT (No. CZ.02.1.01/0.0/0.0/17_048/0007376). Authors

thank to Prof. Takeshi Aoki (Joint Research Center of High-Technology, Tokyo Polytechnic University, Japan) for development and perfected QFRS on UCPL, to Dr. Cyril Koughia (University of Saskatchewan, Canada) for discussion on radiation trapping processes and to Dr. Roman Svoboda (University of Pardubice, Czech Republic) for the differential scanning calorimetry measurements.

References

[1] A. B. Seddon. *J. Non-Cryst. Solids* **184**, 44 (1995).
[2] N. F. Mott, E. A. Davis. *Electronic Processes in Non-Crystalline Materials*, Clarendon Press, Oxford (1997).
[3] R. Fairman, B. Ushkov. *Semiconducting Chalcogenide Glass II: Properties of Chalcogenide Glasses*, Elsevier Inc., San Diego (2004).
[4] T. H. Lee, S. I. Simdyankin, J. Hegedus, J. Heo, S. R. Elliott. *Phys. Ref. B* **81**, 104204 (2010).
[5] R. Fairman, B. Ushkov. *Semiconducting Chalcogenide Glass III: Application of Chalcogenide Glasses*, Elsevier Inc., San Diego (2004).
[6] L. Ying, Ch. Lin, Y. Xu, Q. Nie, F. Chen, S. Dai. *Opt. Mater.* **33**, 1775 (2011).
[7] L. Strizik, J. Hrabovsky, T. Wagner, T. Aoki. *Phil. Mag. Lett.* **95**, 466 (2015).
[8] L. Strizik, J. Zhang, T. Wagner, J. Oswald, T. Kohoutek, B. M. Walsh, J. Prikryl, R. Svoboda, C. Liu, B. Frumarova, M. Frumar, M. Pavlista, W. J. Park, J. Heo. *J. Lumin.* **147**, 209 (2014).
[9] Y. G. Choi, K. H. Kim, B. J. Lee, J. B. Shin, Y. S. Kim, J. Heo. *J. Non-Cryst. Solids* **278**, 137 (2000).
[10] C. C. Ye, D. W. Hewak, M. Hempstead, B. N. Samson, D. N. Payne. *J. Non-Cryst. Solids* **208**, 56 (1996).
[11] X. F. Wang, X. J. Zhao, Z. W. Wang, H. T. Guo, S. X. Gu, J. G. Yu, C. L. Liu, Q. H. Gong. *Mater. Sci. Eng. B* **110**, 38 (2004).
[12] S. Kasap, K. Koughia, G. Soundararajan, M. G. Brik. *IEEE. J. Sel. Top. Quant.* **14**, 1353 (2008).
[13] J. Zavadil, M. Kubliha, P. Kostka, M. Iovu, V. Labas, Z. G. Ivanova. *J. Non-Cryst. Solids* **377**, 85 (2013).
[14] J. Troles, Y. Niu, C. Duverger-Arfuso, F. Smektala, L. Brilland, V. Nazabal, V. Mozain, F. Desevedavy, P. Houizot. *Mater. Res. Bull.* **43**, 976 (2008).
[15] F. Prudenzano, L. Mescia, L. Allegretti, M. De Sario, F. Smektala, V. Mozain, V. Nazabal, J. Troles, J. L. Doualan, G. Canat, J. L. Adam, B. Boulard. *Opt. Mater.* **31**, 1292 (2009).
[16] A. V. Rode, A. Zakery. *Appl. Surf. Sci.* **197–198**, 481 (2002).
[17] F. Prudenzano, L. Mescia, L. Allegretti, V. Mozain, V. Nazabal, F. Smektala. *Opt. Mater.* **33**, 241 (2010).
[18] F. Prudenzano, L. Mescia, L. Allegretti, M. De Sario, T. Palmisano, F. Smektala, V. Mozain, V. Nazabal, J. Troles. *J. Non-Cryst. Solids* **355**, 1145 (2009).
[19] R. Jha, A. K. Sharma. *Opt. Lett.* **34**, 749 (2009).
[20] A. K. Sharma, R. Jha. *J. Appl. Phys.* **106**, 103101 (2009).
[21] A. Schulte, W. Schirmacher, B. Schmid, T. Unruh. *J. Phys.-Condens. Mat.* **23**, 254212 (2011).
[22] M. Wojdyr. *J. Appl. Crystallogr.* **43**, 1126 (2010).
[23] W. Sellmeier. *Ann. Phys. Chem.* **143**, 272 (1871).
[24] L. Strizik, V. Prokop, J. Hrabovsky, T. Wagner, T. Aoki. *J. Mater. Sci.-Mater. El.* **28**, 7053 (2017).
[25] T. Aoki, L. Strizik, J. Hrabovsky, T. Wagner. *J. Mater. Sci.-Mater. El.* **28**, 7077 (2017).
[26] C. Koughia, M. G. Brik, G. Soundararajan, S. Kasap. *J. Non-Cryst. Solids* **377**, 90 (2013).
[27] S. O. Kasap, K. Koughia, M. Munzar, D. Tonchev, D. Saitou, T. Aoki. *J. Non-Cryst. Solids* **353**, 1364 (2007).
[28] J. Heo, J. M. Yoon, S. Y. Ryou. *J. Non-Cryst. Solids* **238**, 115 (1998).
[29] C. Maurel, L. Petit. *J. Solid State Chem.* **181**, 2869 (2008).
[30] M. Ichikawa, T. Wakasugi, K. Kadono. *J. Non-Cryst. Solids* **356**, 2235 (2010).
[31] Y. Ledemi, S. H. Messaddeq, I. Skhripachev, S. J. L. Ribeiro, Y. Messaddeq. *J. Non-Cryst. Solids* **355**, 1884 (2009).
[32] T. Petkova, B. Monchev, O. Kostadinova, P. Petkov, S. N. Yannopoulos. *J. Non-Cryst. Solids* **355**, 2063 (2009).
[33] F. Kyriazis, A. Chrissanthopoulos, V. Dracopoulos, M. Krbal, T. Wagner, M. Frumar, S. N. Yannopoulos. *J. Non-Cryst. Solids* **355**, 2010 (2009).
[34] C. Koughia, S. O. Kasap. *J. Mater. Sci.-Mater. El.* **20**, 139 (2009).
[35] C. Koughia, C. Craig, D. W. Hewak, S. Kasap. *Opt. Mater.* **9**, 2368 (2019).
[36] A. Ravagli, N. G. Boetti, F. A. Guzman Cruz, G. A. Alzaidy, D. Pugliese, D. Milanese, D. W. Hewak. *RSC Adv.* **8**, 27556 (2018).
[37] G. A. Kumar, E. De la Rosa, H. Desirena. *Opt. Comm.* **260**, 601 (2006).
[38] F. Liu, E. Ma, D. Chen, Y. Yu, Y. Wang. *J. Phys. Chem. B* **110**, 20843 (2006).
[39] Z. G. Ivanova, Z. Aneva, R. Ganesan, D. Tonchev, E. S. R. Gopal, K. S. R. K. Rao, T. W. Allen, R. G. DeCorby, S. O. Kasap. *J. Non-Cryst. Solids* **353**, 1418 (2007).
[40] H. Guo, N. Dong, M. Yin, W. Zhang, L. Lou, S. Xia. *J. Phys. Chem. B* **108**, 19205 (2004).
[41] G. Y. Chen, H. J. Liang, H. C. Liu, G. Somesfalean, Z. G. Zhang. *J. Appl. Phys.* **105**, 114315 (2009).

[42] Y. Zhang, J. Hao, C.L. Mak, X. Wei. *Opt. Express* **19**, 1824 (2011).
[43] A. Miguel, R. Morea, J. Gonzalo, M. A. Arriandiaga, J. Fernandez, R. Balda. *J. Lumin.* **140**, 38 (2013).
[44] D. R. Gamelin, H. U. Güdel. *Upconversion Processes in Transition Metal and Rare Earth Metal System in Transition Metal and Rare Earth Compounds*, H. Yersin (Ed.), pp. 1–56. Springer Berlin Heidelberg, Berlin (2001).
[45] R. Martín-Rodríguez, F. T. Rabouw, M. Trevisani, M. Bettineli, A. Meijerink. *Adv. Opt. Mater.* **3**, 558 (2015).
[46] P. Goldner, F. Auzel. *J. Appl. Phys.* **79**, 7972 (1996).
[47] B. M. Walsh. *Judd-Ofelt Theory: Principles and Practices In Advances in Spectroscopy for Lasers and Sensing*, B. Di Bartolo, O. Forte (Eds.), pp. 403–433, Springer, Netherlands (2006).
[48] M. P. Hehlen, M. G. Brik, K. W. Krämer. *J. Lumin.* **136**, 221 (2013).
[49] B. R. Judd. *Phys. Rev.* **127**, 750 (1962).
[50] G. S. Ofelt. *J. Chem. Phys.* **37**, 511 (1962).
[51] G. A. Kumar, E. De la Rosa, H. Desirena. *Opt. Comm.* **260**, 601 (2006).
[52] F. Liu, E. Ma, D. Chen, Y. Yu, Y. Wang. *J. Phys. Chem. B* **110**, 20843 (2006).
[53] J. P. Wittke, I. Ladany, P. N. Yocom. *J. Appl. Phys.* **43**, 595 (1972).
[54] F. Vetrone, J-C. Boyer, J. A. Capobianco. *Chem. Mater.* **15**, 2737 (2003).
[55] F. Vetrone, J-C. Boyer, J. A. Capobianco. *J. Appl. Phys.* **96**, 661 (2004).
[56] X. Yin, H. Wang, M. Xing, Y. Fu, Y. Tian, T. Jiang, X. Luo. *J. Lumin.* **182**, 183 (2017).
[57] F. Huang, L. Hu, D. Chen. *Ceram. Int.* **41**, 189 (2015).
[58] X. Yin, H. Wang, M. Xing, Y. Fu, Y. Tian, X. Shen, W. Yu, X. Luo. *J. Rare Earth.* **35**, 230 (2017).
[59] K. V. Krishnaiah, P. Venkatalakshmamma, Ch. Basavapoornima, I. R. Martin, K. Soler-Carracedo, M. A. Hernandez-Rodriguez, V. Venkatramu, C. K. Jayasankar. *Mater. Chem. Phys.* **199**, 67 (2017).
[60] Ch. Mi, J. Wu, Y. Yang, B. Han, J. Wei. *Sci. Rep.* **6**, 22545 (2016).